Deformation mechanism of ZK61 magnesium alloy cylindrical parts with longitudinal inner ribs during hot backward flow forming

Qinxiang Xia[a], Jinchuan Long[a,b*], Gangfeng Xiao[a], Shuai Yuan[a], Yi Qin[b*]

(a. School of Mechanical and Automotive Engineering, South China University of Technology, Guangzhou 510640, China; b. Centre for Precision Manufacturing, DMEM, University of Strathclyde, Glasgow G1 1XQ, UK)

Abstract: Thin-walled cylindrical parts with longitudinal inner ribs (CPLIRs) made of magnesium (Mg) alloys are one of the most promising lightweight components for industrial applications. Flow forming is an effective technology to realize the integrated manufacturing of thin-walled CPLIRs. However, due to the complicated material flow and narrow temperature window, defects such as insufficient filling at the rib groove and concavity of the back of the rib occur easily during hot backward flow forming (HBFF) of ZK61 Mg alloy thin-walled CPLIRs. The isothermal uniaxial compression test was proposed as the physical simulation test of the HBFF of thin-walled CPLIRs, and a novel method for analyzing the formability of hot spin-forming was proposed on the basis of the combination of 3D hot processing maps (HPMs) and 3D finite element (FE) simulation. The process experiment and 3D FE simulation integrated with 3D HPMs were conducted to investigate the deformation characteristic and material flow, and the formation mechanism of defects was then revealed. Further, the influence of process parameters on the power dissipation efficiency of spun workpiece was discussed. The results show that safe deformation of the alloy is concentrated at a narrow region with high temperature and low strain rate; the large tangential flow at the cylindrical wall and radial flow at the inner rib contributed to the filling of rib groove; unsaturated inner rib and concavity of the outer wall at the back of the rib are typical defects; the ZK61 alloy CPLIRs exhibits good formability during HBFF under reasonable process parameters, which is beneficial for obtaining qualified forming quality and uniform recrystallized microstructure.

Key words: Magnesium alloy; Cylindrical parts with longitudinal inner ribs; Hot backward flow forming; Deformation mechanism

---

* Corresponding author.
E-mail addresses: long.jc@mail.scut.edu.cn (J.C. Long), qin.yi@strath.ac.uk (Y. Qin)

Nomenclature

σ	Flow stress	D	Dissipation function
σ_r	Radial stress	ξ	Instability parameter
σ_θ	Tangential stress	ψ_t	Thinning ratio of wall thickness
σ_a	Axial stress	Δ	Radial feed of roller
ε	Plastic strain	f	Roller feed rate
ε_r	Radial strain	T	Forming temperature
ε_θ	Tangential strain	μ	Saturation degree of inner rib
ε_a	Axial strain	S_a	Actual cross-section area of inner rib
$\dot{\varepsilon}$	Strain rate	S_t	Theoretical cross-section area of inner rib
$\dot{\varepsilon}_{min}$	Minimum strain rate	λ	Inhomogeneity degree of rib height
P	Total absorbed energy	h	Ideal filling height of inner rib
G	Dissipation content	h_{max}	Maximum filling height of inner rib
J	Dissipation co-content	h_{min}	Minimum filling height of inner rib
J_{max}	Maximum dissipation co-content	γ	Concave ratio of the back of the rib
m	Strain-rate sensitivity exponent	R_w	Outer radius of cylindrical wall
K	Material constant	R_r	Outer radius of inner rib
η	Efficiency of power dissipation		

1. Introduction

Thin-walled cylindrical parts with longitudinal inner ribs (CPLIRs) have been widely used in the aerospace field, such as hypersonic vehicles and launch vehicles, due to the enhanced stiffness and strength (Zeng et al., 2018). Magnesium (Mg) alloys with low density and high strength-to-weight ratio have great potential in the lightweight of components and structures, and thus thin-walled CPLIRs made of Mg alloys have increasingly drawn attention in aerospace products (Yuan et al., 2020). However, Mg alloys exhibit poor workability at room temperature because of the hexagonal close-packed crystal structure and low tendency to twinning (Ramezani et al., 2014). In addition, Mg alloys have a high temperature sensitivity and a narrow hot processing window which make defects like cracking and peeling occur

easily during the hot forming processes (such as rolling, forging, extrusion and spinning) (Liu et al., 2016). These factors severely restrict the applications and development of Mg alloy thin-walled CPLIRs.

As a powerful tool for characterizing the material workability, hot processing maps (HPMs) which consist of power dissipation maps and flow instability maps have been successfully applied in a wide range of materials (Wang et al., 2014). As for the HPMs of Mg alloys, Slooff et al. (2010) constructed the 2D HPMs of AZ41, AZ61, and AZ80 alloys, and results show that uniform microstructure with dynamic recrystallization (DRX) was obtained under a strain rate of $5s^{-1}$ and temperatures of 648K for AZ41 and 598K for AZ61 and AZ80. Shang et al. (2015) constructed the 2D HPMs of AZ31 alloy, and the optimum deformation parameters were obtained at 573 ~ 623K and 0.01-$1s^{-1}$. The traditional 2D HPMs are independent of the strain, while the hot deformation of Mg alloys is highly sensitive to not only temperature and strain rate but also strain (Long et al., 2021). Hence, the use of 3D HPMs considering the effect of strain factor on workability has attracted much attention of researchers. To date, the literature on 3D HPMs of Mg alloys mainly focuses on AZ series alloys (Zeng et al., 2019), only Li et al. (2014) established the 3D HPMs of ZK60 and found that the power dissipation efficiency and flow instability regions vary as strain increases.

In recent years, the finite element (FE) simulation as an effective approach to design and optimize forming processes (Yang et al., 2020), has been increasingly combined with HPMs to analyze the formability of hot deformation (Liu et al., 2013). Jin et al. (2018) conducted the FE simulation including 2D HPMs of AZ31B for hot forging of a straight spur gear by Marc software, and the forged gear with good tooth filling and fine-grained microstructure was produced within the safe deformation domain. Zeng et al. (2020a) integrated the 3D HPMs of Mg-8Gd-3Y alloy into Deform-3D software and simulated the hot extrusion of a flat bottom cylindrical part, and the flanged workpiece formed with good surface quality and relatively uniform microstructures and mechanical properties was obtained under optimized process parameter. With respect to metal spinning, Xiao et al. (2018) constructed the 2D HPMs of Haynes 230 alloy by an isothermal plane strain compression and guided the selection of process parameters for the hot flow forming experiment of cylindrical parts. However, the distributions of temperature, strain rate and strain at various locations are different and constantly change during

the spinning process. Therefore, it is hard to analyze the formability of spun workpiece accurately merely relying on HPMs, while the FE simulation integrated with HPMs has not been applied to hot spin-forming to the best of our knowledge.

The traditional forming methods of thin-walled cylindrical parts with inner ribs (CPIRs) include milling, casting, and welding, where the material utilization ratio and work efficiency are difficult to guarantee and mechanical properties of the formed CPIRs are weakened (Zeng et al., 2020b). With the enhanced formability, low deformation resistance, and high forming precision (Xiao et al. 2018), the forming technology of hot backward flow forming (HBFF) was proposed to realize the integrated manufacturing of Mg alloy thin-walled CPLIRs by Yuan et al. (2020). However, the material flow during the flow forming process of CPLIRs is extremely complicated (Ma et al., 2010). Not only the deformed material flows along the radial and axial directions, but also the wall-thickness of CPLIRs along a circumferential direction is periodically changed due to the existence of inner ribs (Xia et al., 2014). Also, the large linear expansion coefficient and thermal conductivity of Mg alloys make it difficult to control the temperature and deformation uniformity of the CPLIRs during the HBFF (Yuan et al., 2020). These influence factors are responsible for the occurrence of defects such as insufficient filling of rib groove and concavity of the back of the rib, and the uneven microstructure between the cylindrical wall and the inner ribs. Therefore, it is highly necessary to reveal the deformation mechanism of Mg alloy thin-walled CPLIRs during the HBFF process, to achieve the integrated control of forming quality and microstructure evolution.

To date, some efforts have been made to investigate the spinning process of thin-walled CPIRs by numerical simulation and experiment. Jiang et al. (2009) studied the backward ball spinning of 5A02 aluminum (Al) alloy thin-walled CPLIRs, and found that the spinning force increases with increasing spinning pass. Zeng et al. (2020c) analyzed the flow forming of 6061 Al alloy thin-walled cylindrical parts with cross inner ribs and revealed the die filling mechanism. The results show that the occurrence of folding causes a poor surface quality and the rib height can be improved by increasing the thinning ratio and roller feed rate. Xu et al. (2016) studied the stagger spinning of an internally toothed gear, and found that the main defects were underfilling and cracking occurred in the vicinity of the teeth. Moreover, Xia et al. (2011) researched the stagger spinning of Q235 cup-shaped

thin-walled inner gears, and found that thinning ratio is the dominant factor for the filling height of the gear teeth. Recently, Yuan et al. (2020) experimentally analyzed the HBFF process of ZK61 alloy thin-walled CPLIRs, and found that the microstructure at both the cylindrical wall and the inner ribs can be refined after spinning. However, there was still a lack of clear understanding about the deformation mechanism of Mg alloy thin-walled CPLIRs during the HBFF.

In this paper, the process experiment and 3D FE simulation integrated with 3D HPMs were carried out to investigate the deformation mechanism of an extruded Mg-Zn-Zr alloy thin-walled CPLIRs during the HBFF process. The deformation characteristics and material flow of spun workpiece were analyzed, and the distribution of power dissipation efficiency was discussed. Eventually, the formation mechanism of defects was revealed, the forming quality of thin-walled CPLIRs was evaluated, and the method for analyzing the formability of hot spin-forming was validated. The research results will provide guidance for the shape/property integrated control of the hot flow forming of Mg alloy CPLIRs.

2. Experimental and modeling procedures

2.1 Physical simulation test of HBFF of CPLIRs

Fig. 1 shows the schematic illustration of the HBFF of thin-walled CPLIRs, where the three-roller stagger spinning was used for balancing the spinning force of rollers and improving the forming efficiency (Xia et al., 2014). During the HBFF process, the mandrel and snap ring rotate with the spindle of the spinning machine, the blank is driven by friction between it, the snap ring and the mandrel, and each roller feeds along axial and radial directions to form the inner ribs. The induction heating with a high heating rate and high energy efficiency was adopted (Xiao et al., 2018). The deformation zones in flow forming of thin-walled CPLIRs can be divided into two parts, i.e., the inner rib (zone A) and the cylindrical wall (zone B), as shown in Fig. 2, where the states of stress and strain is described. It is found that the deformed material of the cylindrical wall and that of the inner rib are both in a state of three-directional compressive stress (Zeng et al., 2020c). It also can be seen from Fig. 2 that two tensile strains and one compressive strain exist at both of the cylindrical wall and the inner rib (Jiang et al., 2009), which is similar to the strain state of the uniaxial compression test. Therefore, the isothermal uniaxial

compression test was proposed as the physical simulation test of the HBFF of thin-walled CPLIRs, to obtain the relationship between the large true strain and stress of ZK61 alloy during the HBFF.

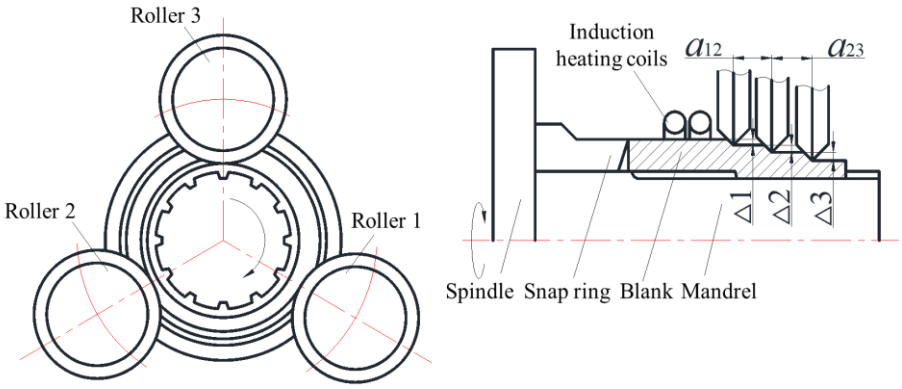

Fig. 1. Schematic illustration of the HBFF of thin-walled CPLIRs.

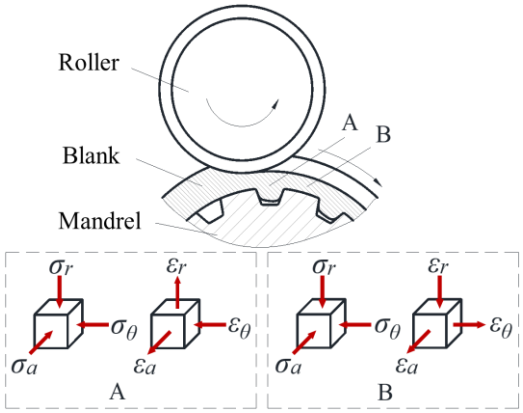

Fig. 2. States of stress and strain during the backward flow forming of thin-walled CPLIRs.

The studied ZK61 alloy with a composition of Mg-5.42Zn-0.58Zr (in wt.%) in the present work is identical to that reported in a previous publication (Long et al., 2021). Fig. 3 shows the initial microstructure, in which there are not only some fine DRX grains with an average grain size of 2.5μm, but also some long-strip shaped grains elongated along the extrusion direction (ED). A series of isothermal uniaxial compression tests were carried out at temperatures of 523 ~ 673K and strain rates of 0.001~1s^{-1} on the Gleeble-3500 thermo-mechanical simulator. The total deformation degree of compression samples was set as 70%, and the obtained true strain can reach about 1.2. More details about the test method and results can be found in Long et al. (2021).

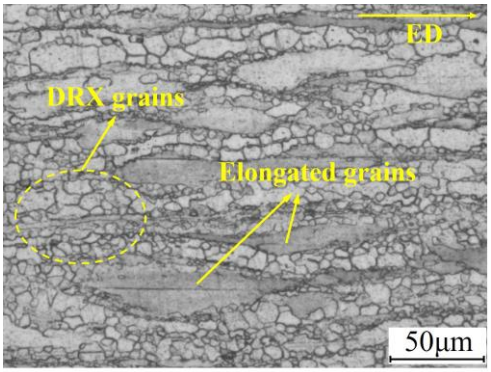

Fig. 3. Optical micrograph of initial microstructure.

2.2 Construction of 3D HPMs

2.2.1 Power dissipation map

The HPMs in this study was constructed on the basis of the dynamic material model, where the hot deformation was considered as the power dissipation process, and the absorbed energy P per unit volume includes two complementary parts (Zhong et al., 2013):

$$P = \sigma \cdot \dot{\varepsilon} = G + J = \int_0^{\dot{\varepsilon}} \sigma d\dot{\varepsilon} + \int_0^{\sigma} \dot{\varepsilon} d\sigma \tag{1}$$

where, the content G is the power dissipated by plastic deformation, while the co-content J is the power dissipated by microstructure evolution. Under a given strain and temperature, the sensitivity coefficient of strain rate m can be expressed as follows (Quan et al., 2011):

$$\frac{\partial J}{\partial G} = \frac{\dot{\varepsilon}\partial\sigma}{\sigma\partial\dot{\varepsilon}}\Big|_{\varepsilon,T} = \frac{\partial \ln\sigma}{\partial \ln\dot{\varepsilon}}\Big|_{\varepsilon,T} = m \tag{2}$$

The relationship between the flow stress and strain rate satisfies a power law, which can be expressed as follows (Liu et al., 2008):

$$\sigma = K \cdot \dot{\varepsilon}^{m} \tag{3}$$

where, the K is the material constant. Combined with Eqs. (1) and (3), the efficiency of power dissipation η which represents the power dissipation capacity of material can be defined as follows (Shalbafi et al., 2017):

$$\eta = \frac{J}{J_{\max}} \tag{4}$$

where, $J_{max}=P/2$ in an ideal linear dissipator, and then the efficiency of power

dissipation η can be thus calculated as follows:

$$\eta=\frac{2J}{P}=\frac{2m}{m+1} \tag{5}$$

However, it is suggested that the Eq. (5) is not appropriate for materials with complicated flow stress curves which do not follow the power law (Murty et al., 1998a), while ZK61 alloy exhibits complex variation tendencies as strain increases during the hot deformation as reported in Malik et al. (2020). Therefore, the η of such material should be calculated according to the numerical integration procedure, which can be expressed as follows:

$$\eta=2\left[1-\frac{1}{\sigma\dot{\varepsilon}}\int_0^{\dot{\varepsilon}}\sigma d\dot{\varepsilon}\right] \tag{6}$$

Since the experimental data before the minimum strain rate are normally considered to have no applicability, the dissipation content G was further divided into two parts, which can be described as follows:

$$G=\int_0^{\dot{\varepsilon}_{\min}}\sigma d\dot{\varepsilon}+\int_{\dot{\varepsilon}_{\min}}^{\dot{\varepsilon}}\sigma d\dot{\varepsilon}=\left(\frac{\sigma\dot{\varepsilon}}{m+1}\right)_{\dot{\varepsilon}=\dot{\varepsilon}_{\min}}+\int_{\dot{\varepsilon}_{\min}}^{\dot{\varepsilon}}\sigma d\dot{\varepsilon} \tag{7}$$

where, $\dot{\varepsilon}_{\min}$ is the smallest strain rate during the isothermal compression test. The first integration term satisfies the power law, and the second integration term can be calculated by the numerical integration of a cubic spline fit for flow stress within the experimental data. Therefore, the η of the material was calculated as follows:

$$\eta=2\left[1-\frac{1}{\sigma\dot{\varepsilon}}\left(\left(\frac{\sigma\dot{\varepsilon}}{m+1}\right)_{\dot{\varepsilon}=\dot{\varepsilon}_{\min}}+\int_{\dot{\varepsilon}_{\min}}^{\dot{\varepsilon}}\sigma d\dot{\varepsilon}\right)\right] \tag{8}$$

The different values of η correspond to different microscopic mechanisms within safe regions such as dynamic recovery (DRV), DRX, or superplasticity (Shang et al., 2015). Based on the obtained flow stress data, the values of η under various temperatures, strain rates and strains were calculated. The 3D power dissipation map was thus constructed by plotting a contour map of the parameter η under different strains. Fig. 4 shows that the grid color of each point represents the power dissipation efficiency. The higher the η value, the larger the proportion of the energy dissipated by microstructure evolution (Du et al., 2015). The η value changes greatly with increasing strain. At low strain rate and low temperature, the η value

decreases obviously as strain increases. Moreover, the η value within 573 ~ 673K and 0.001-0.01s^{-1} is about 35~45%, suggesting that DRX occurs easily in the region. The microstructure obtained at 573K/0.001s^{-1} and 623K/0.001s^{-1} was observed. Fig. 5 shows the grain refinement caused by DRX is remarkable, and the initial microstructure can be basically replaced by DRX grains. Since the DRX can not only provide stable flow and good formability but also reconstitute microstructure, the region with the occurrence of DRX can be regarded as a priority for hot deformation of the ZK61 alloy.

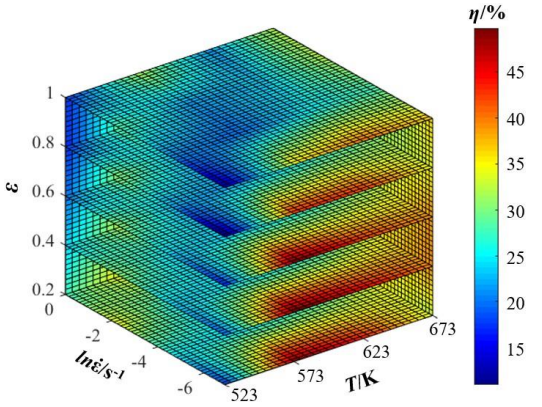

Fig. 4. 3D power dissipation map.

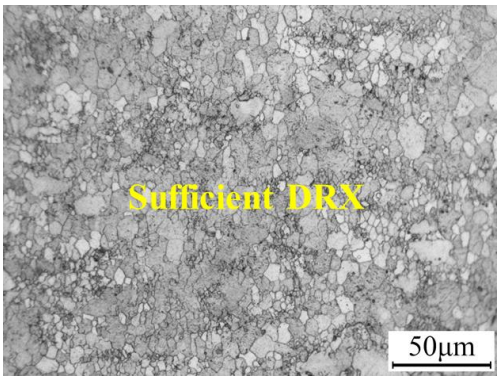

Fig. 5. Optical microstructure at 573K/0.001s^{-1}.

2.2.2 Flow instability map

A 3D flow instability map is also necessary for characterizing the workability comprehensively besides the power dissipation map (Wang et al., 2015). The instability criterion was selected due to its extensive applicability (Murty et al., 1998b). This criterion is developed on the basis of the continuum theory of large plastic deformation, and the extremum principles of irreversible thermodynamics are satisfied, the expression can be given as follows:

$$\frac{\partial D}{\partial \dot{\varepsilon}} < \frac{D}{\dot{\varepsilon}} \tag{9}$$

where, D is the dissipation function related to the flow behavior of the material, which can be replaced by J, and thus Eq. (9) can be expressed as follows:

$$\frac{\partial J}{\partial \dot{\varepsilon}} < \frac{J}{\dot{\varepsilon}} \tag{10}$$

Combined with Eqs. (1-2) and (4), the equations can be obtained as follows:

$$\frac{\partial J}{\partial \dot{\varepsilon}} = \frac{\partial \sigma}{\partial \dot{\varepsilon}} \dot{\varepsilon} = \sigma \frac{\partial \ln \sigma}{\partial \ln \dot{\varepsilon}} = \sigma m \tag{11}$$

$$\frac{J}{\dot{\varepsilon}} = \frac{1}{2} \eta \sigma \tag{12}$$

According to the Eqs. (10-12), the instability parameter can be expressed as:

$$\xi(\dot{\varepsilon}) = 2m - \eta < 0 \tag{13}$$

Based on calculated values of the instability parameter under different strains, the 3D flow instability map of ZK61 alloy was constructed as shown in Fig. 6, where the black areas represent the flow instability regions and the grey areas represent the safe regions. It can be seen from Fig. 6 that the flow instability region occurred at low temperature and high strain rate is influenced by temperature, strain and strain rate, which mainly appears in the temperature range of 523 ~ 543K and strain rate range of 0.3-1s^{-1} when the strain reaches 1.0. The microstructure at 523K/1s^{-1} was observed. As shown in Fig. 7, the small DRX grains nucleate at the original grain boundaries and provide a path for the slip at low temperature and high strain rate, which results in a concentrated deformation and the flow localization bands in the region. This is not beneficial to improving the material workability (Li et al., 2014). Therefore, the optimized hot deformation parameters of the alloy can be obtained at temperatures of 573~ 673K and strain rates of 0.001-0.01s^{-1}.

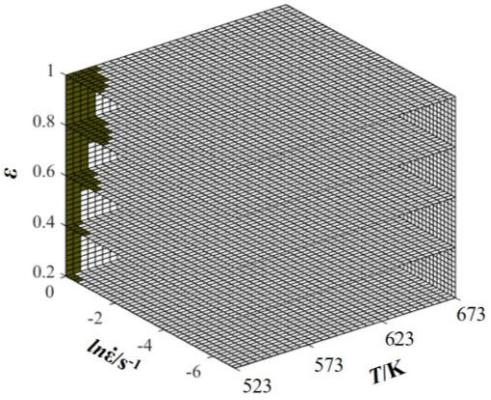

Fig. 6. 3D flow instability map.

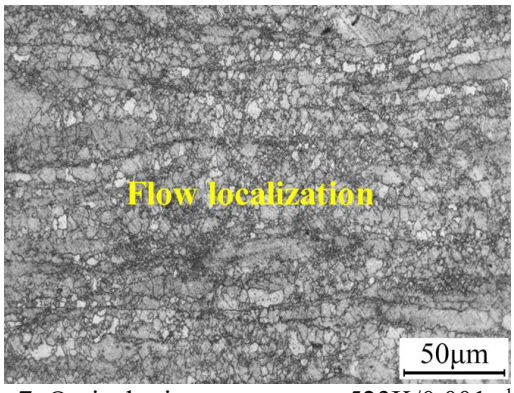

Fig. 7. Optical microstructure at 523K/0.001s^{-1}.

2.3 Experimental details

The cylindrical blank with an inner diameter of 60mm and a wall thickness of 8mm was used in the experiment (Fig. 8), and the structure design of the target part is in line with JB/T9177-1999 of China. The longitudinal inner ribs are symmetrically distributed and the total number is selected as 12, the multiple of the

number of rollers, to guarantee the steady movement of rollers during the HBFF process. Considering the thermal expansion and contraction of the cylindrical blank and mandrel under the heating condition, the diameter of the mandrel was designed as 59.8mm. The commonly adopted double-tapered roller was chosen for realizing the uniform filling of inner ribs during the HBFF and the geometric parameters of the rollers were reported by Yuan et al. (2020).

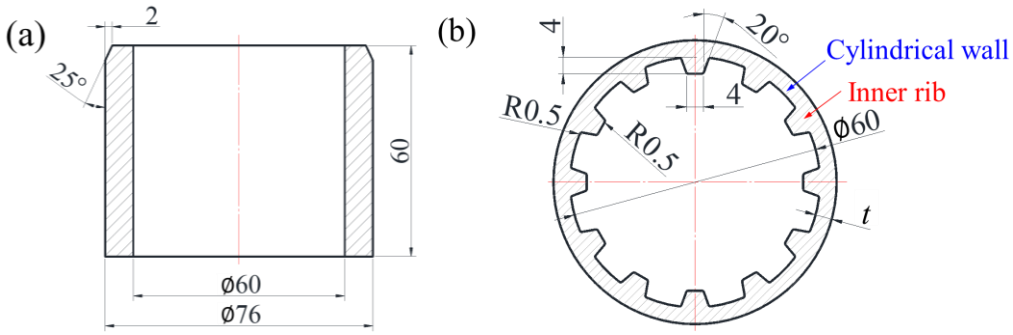

Fig. 8. Structure illustration of (a) initial blank and (b) target part.

The HBFF experiment was carried out on the HGQX vertical hot power spinning machine (Fig. 9), where the induction heating system was used and the automatic temperature measurement and controlling system was adopted, as shown in Fig. 10. Since the hot deformation behaviour of ZK61 alloy is highly sensitive to the temperature, strain rate and strain (Long et al, 2021), the forming temperature T, roller feed rate f, and thinning ratio of wall-thickness ψ_t, were chosen as the process parameters in the work. Combining with the results of previous work (Yuan et al., 2020), the experimental and simulation scheme was designed on the basis of the constructed 3D HPMs of the ZK61 alloy (Table 1).

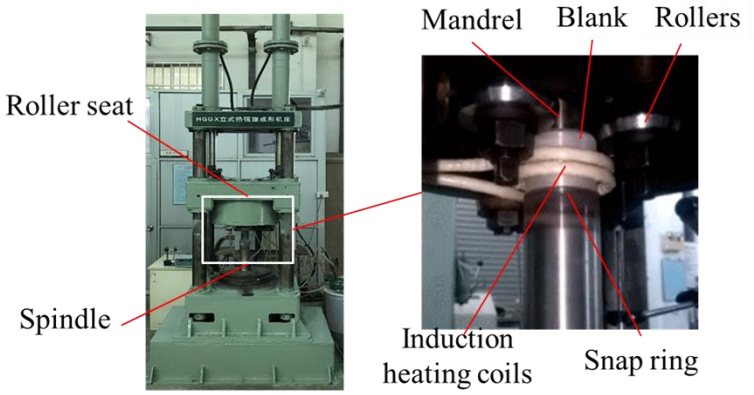

Fig. 9. HGQX hot power spinning machine.

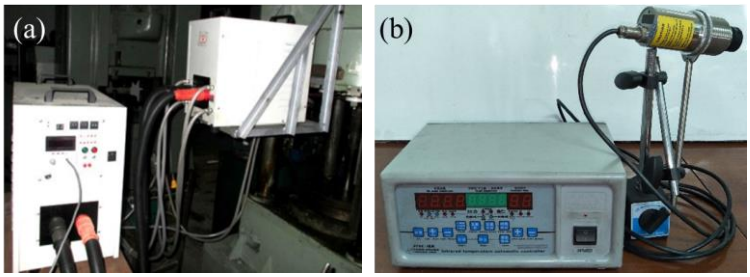

Fig. 10. Experimental devices: (a) induction heating system (b) temperature measurement and controlling system.

Table 1 Process parameters for HBFF of ZK61 alloy thin-walled CPLIRs.

Thinning ratio of wall thickness ψ_t/%	Radial feed of roller Δ/mm	Roller feed rate f/(mm/r)	Forming temperature T/K
50	4/(1.4, 1.35, 1.25)	0.4, 0.6, 0.8, 1.0	523, 573 623, 673
55	4.4/(1.5, 1.45, 1.45)		
60	4.8/(1.65, 1.6, 1.55)		
65	5.2/(1.8, 1.75, 1.65)		

2.4. FE modelling integrated with 3D HPMs

Fig. 11 shows the geometric model of the HBFF of ZK61 alloy thin-walled CPLIRs established by Abaqus/Explicit software. The cylindrical blank was treated as a deformable body, the rollers and mandrel were defined as rigid bodies. It should be noted that the filling of rib groove is greatly influenced by the mesh size during the simulation process (Wong et al., 2004). Since the mesh size of the cylindrical blank along the circumferential direction should be close to the radius of the rib groove, the circumference was equally divided into 1.8 degrees and 200 elements were obtained, where the mesh sizes of the inner and outer surfaces were 0.92mm and 1.16mm, respectively. The mesh size of 1mm in the thickness direction and axial direction was chosen to guarantee the forming accuracy and simulation efficiency. The total number of elements is 72000 and the ratio of maximum element length to minimum element length is close to the ideal value 1. The reduced integration brick element for the coupled temperature-displacement analysis (C3D8RT) was adopted (Mohamed et al., 2012), and the enhanced hourglass control was used to avoid the hourglass phenomenon.

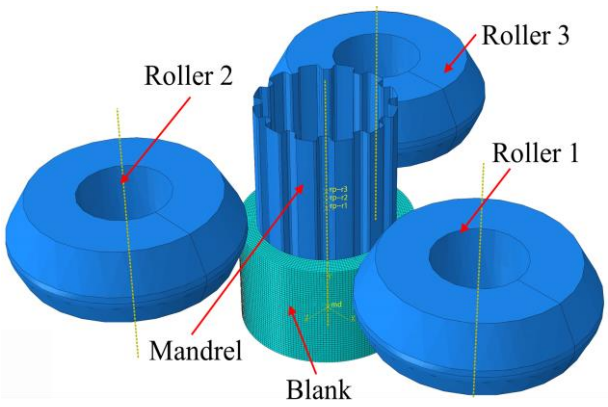

Fig. 11. Geometric model of HBFF of ZK61 alloy thin-walled CPLIRs.

A numerical error could occur due to a large-scale rotation of a deformable body, and thus the cylindrical blank and mandrel were fixed and the rollers revolved around the axis of the blank during the simulation process, where the revolving speed of the rollers was equal to the spindle speed (Huang et al., 2011). The isotropy Coulomb friction model was selected, and the friction coefficient between the rollers and the cylindrical blank was 0.1, while that between the blank and the mandrel was 0.15 (Zhang et al., 2019). The obtained stress-strain data in Section 2.1 were imported into the software via a user-defined material library in the form of true stress and plastic strain. Moreover, a mass-scaling factor of 1000 was used to reduce the computing time (Wong et al., 2004). To realize the thermo-mechanical coupling simulation, the thermodynamic parameters of ZK61 alloy were tested by the dynamic thermomechanical analysis (DMA), thermal constant analyzer (Hotdisk), differential scanning calorimetry (DSC) and thermal dilatometer (DIL402PC) (Table 2) and imported into the material library. Additionally, the forming temperature was defined in a predefined field, the film coefficient and emissivity were both defined as 0.1 to realize the convective heat transfer and radiant heat transfer between the cylindrical blank and the outer environment. To analyze the formability of ZK61 alloy thin-walled CPLIRs during the HBFF, the constructed 3D HPMs were integrated into the Abaqus software by the secondary development of the user subroutine using FORTRAN language, and the calculation flowchart of the subroutine is shown in Fig. 12.

Table 2 Thermodynamic parameters of ZK61 alloy

Temperature/(K)	523	573	623	673
Elastic modulus E/(GPa)	24.43	23.45	22.51	20.31
Heat conduction coefficient λ/(W/m • K)	111.8	116.7	120.7	125.3
Specific heat c($\times 10^3$)/(J/Kg • K)	1.28	1.28	1.3	1.33
Thermal expansion coefficient a ($\times 10^{-5}$)/(K)	2.33	2.34	2.39	2.41

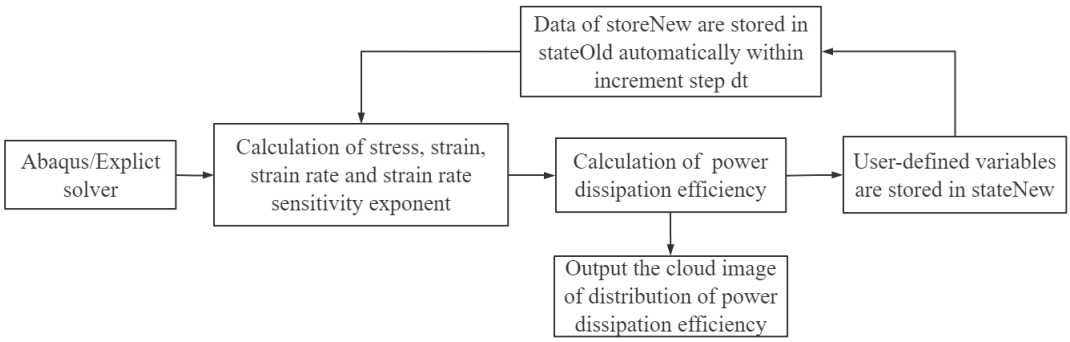

Fig. 12. Calculation flowchart of subroutine for 3D FE simulation integrated with 3D HPMs.

To verify the reliability of the developed FE model, the HBFF experiment was conducted under T=573K, f=0.4mm/r and Ψ_t=60%, which is outside the instability region and belongs to the safety region. The spun workpiece without peeling and cracking was formed, and thus it undergoes safe deformation. However, it can be observed that the wave-shaped opening end occurs during both simulation and experiment where the concavity of the inner ribs exhibits on the outer surface of spun workpiece (Fig. 13(a)). The simulated opening-end and bottom-end of the spun workpiece are close to those of experiment, where the high outside and low inside exhibit along the wall-thickness direction and the rib height at the bottom-end is higher than that at the opening-end (Fig. 13(b)). Therefore, the simulation results are consistent with those of the experiment. Also, eight measuring points with an equal interval along the axial direction of the spun workpiece at the stable stage of HBFF were selected (Fig. 14), and the wall-thickness in the experiment was measured by the ultrasonic thickness gauge. It was found that the simulated values tend to be higher than the experimental ones. It is partially due to that the distance between the two nodes which are not at the same cross-section in the FE model was slightly larger than the actual wall-thickness (Zeng et al., 2020c). But, the maximum relative error between them is 5.3% (Fig. 15), which further indicates that the simulated results of the established FE model are generally acceptable.

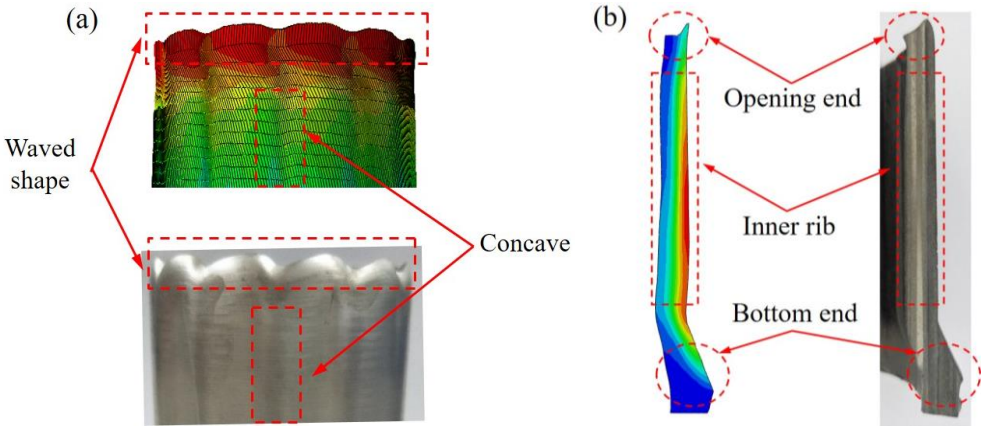

Fig. 13. Results comparison between simulation and experiment: (a) outer surface of spun workpiece (b) longitudinal section of spun workpiece.

Fig. 14. Wall-thickness measuring points along the axial direction.

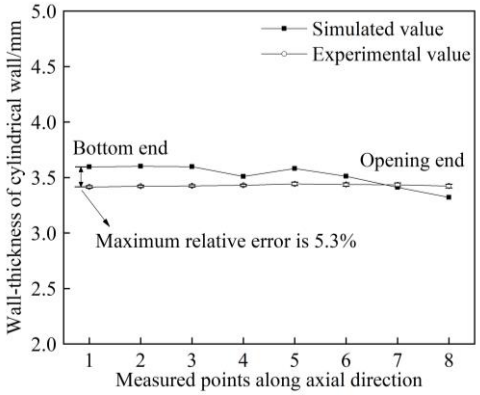

Fig. 15. Distribution of the wall-thickness obtained by simulation and experiment.

2.5 Evaluation method of forming quality

Based on the simulation and experimental results, the forming defects such as the concavity of the outer wall at the back of the rib and insufficient filling at the rib groove occur easily during the HBFF of Mg alloy thin-walled CPLIRs. To evaluate the forming quality of spun workpiece quantitatively, the indexes including the saturation degree of inner rib μ, inhomogeneity degree of rib height λ and the concave ratio of the back of the rib γ were proposed, which can be calculated by Eqs. (14-16).

$$\mu = \frac{S_a}{S_t} \times 100\% \tag{14}$$

$$\lambda = \frac{h_{max} - h_{min}}{h} \times 100\% \tag{15}$$

$$\gamma = \frac{R_w - R_r}{R_w} \times 100\% \tag{16}$$

where, S_a and S_t are the actual and theoretical cross-section areas of inner rib,

respectively; h_{max} and h_{min} are the maximum and minimum filling heights of inner rib, respectively; h is the ideal filling height, i.e., the depth of rib groove; R_w and R_r are the outer radii at the cylindrical wall and the inner rib, respectively, which can be described in Fig. 16.

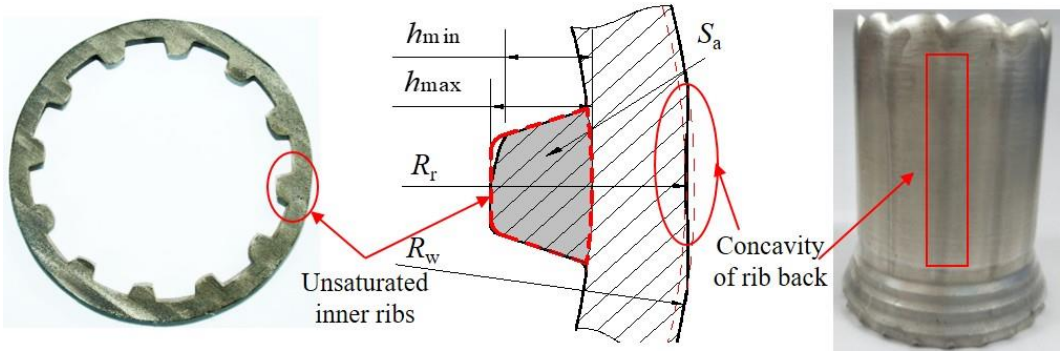

Fig. 16. Illustration of forming defects of Mg alloy thin-walled CPLIRs.

To obtain the outer radii of the thin-walled CPLIRs, eight cross-sections with an equal interval along the axial direction were selected, which are consistent with the position of the measuring points shown in Fig. 14. For each cross-section, the measuring points of the outer radii at the cylindrical wall and the inner rib are distributed evenly along the circumferential direction, as shown in Fig. 17.

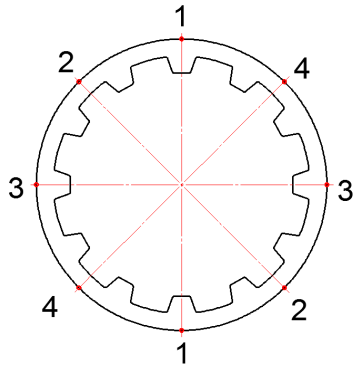

Fig. 17. Measuring points of the outer radii along the circumferential direction.

Additionally, to measure the cross-section area and filling height of inner rib of thin-walled CPLIRs accurately, the method of image measurement and MATLAB software was adopted. Firstly, five cross-sections with an equal interval along the axial direction were obtained from the spun workpiece by wire electrical discharge machining (WEDM) (Fig. 18(a)). Secondly, the cross-section images of spun workpiece were acquired by a digital camera, where the cross physical scale with a fixed length was determined to realize the transformation between pixel coordinates and physical coordinates in MATLAB software (Fig. 18(b)). Thirdly, the developed

image processing algorithm was used to calculate the cross-section area and filling height of the twelve inner ribs for each cross-section (Fig. 18(c)).

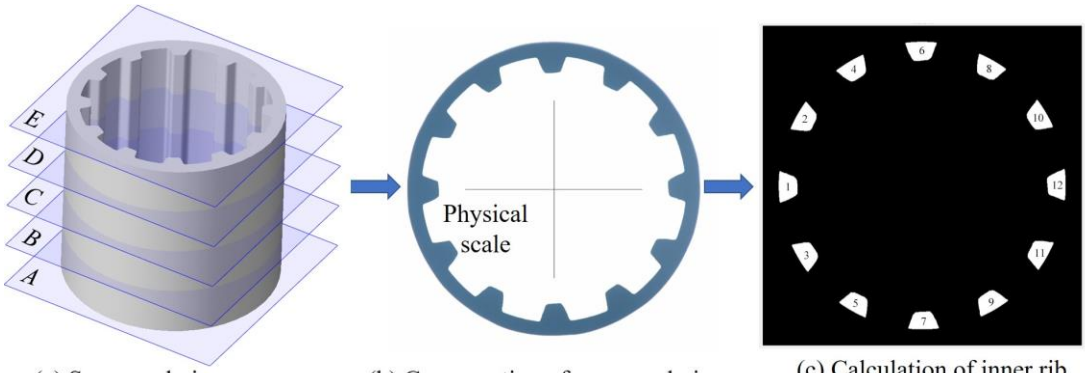

(a) Spun workpiece (b) Cross-section of spun workpiece (c) Calculation of inner rib area and inner rib height

Fig. 18. Image-measurement method for forming quality analysis of thin-walled CPLIRs.

3. Results and discussion

3.1. Deformation characteristic of spun workpiece

Fig. 19 shows the three-directional stress distribution of spun workpiece under T=573K, f=0.4mm/r and Ψ_t=60%. It shows that the contact zone beneath the roller at the cylindrical wall and the inner rib is limited and only concentrates within a small deformation area where the large compressive stress in three directions can be found. Therefore, the deformed material with good ductility is beneficial for the formation of inner ribs (Xiao et al., 2018). The absolute values of stress tend to decrease from the outer surface to the inner surface. This is because the stressed area increases along the local loading direction of rollers, which leads to the decrease of the stress along the wall-thickness direction. It should be noted that the state of stress at the inner layer of the inner rib exhibits differences along three directions where the small tensile stress occurs. This could be the reason that the rib groove has not been fully filled under the thinning ratio, and the inner surface of the blank at the inner rib is still a free surface since there is no restriction caused by a rib groove surface, which is responsible for a small tensile deformation occurring at the inner rib (Zeng et al., 2020c).

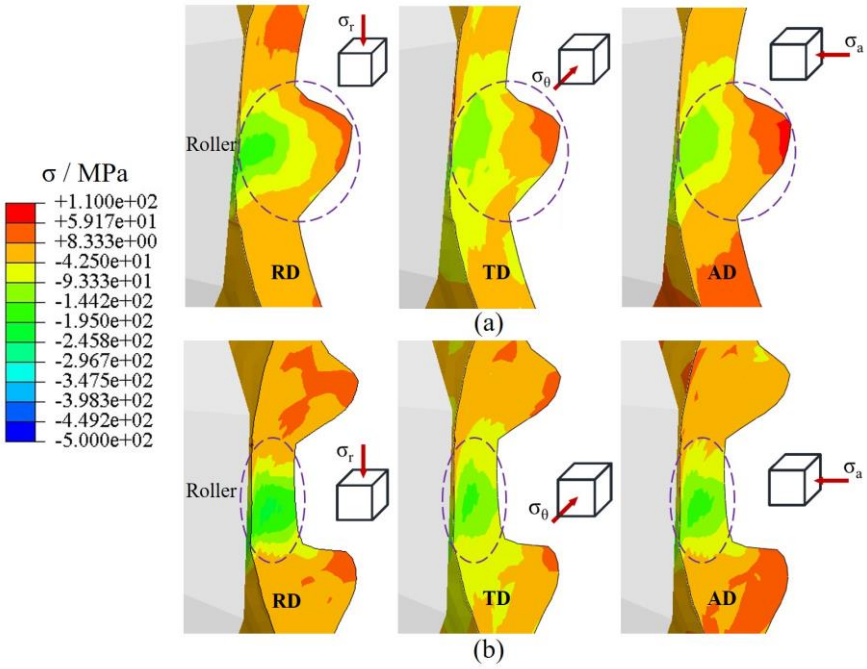

Fig. 19. Stress distribution at the inner rib (a) and the cylindrical wall (b) under T=573K, f=0.4mm/r and Ψ_t=60% (σ_r, σ_θ and σ_a denote the radial, tangential and axial stress respectively; RD, TD and AD denote the radial, tangential and axial direction respectively).

Fig. 20 shows a distribution of the equivalent plastic strain (PEEQ) at a cross-section of the spun workpiece under the same deformation condition, which exhibits the characteristic of periodic distribution. The PEEQ at the cylindrical wall is greater than that at the inner rib, indicating that the deformation degree of the cylindrical wall is larger than that of the inner rib. Therefore, the wave-shaped opening end caused by the differences of deformation degree between the cylindrical wall and the inner rib occurs easily, as shown in Fig. 13(a). The PEEQ decreases from the outer surface to the inner surface along the wall-thickness direction, i.e., the deformation degree at the outer surface is larger than that of the inner surface. It is because the material flow at the inner surface is hindered due to the friction constraint between the blank and the mandrel, and the outer surface of spun workpiece is directly contacted with the rollers and suffers from the applied force, leading to the uneven deformation distribution as well as the phenomenon of high outside and low inside (Fig. 13(b)). Moreover, the metal beneath the inner surface of the spun workpiece is extruded into the groove of the mandrel as a form of rigid and translational motion of the material, which resulted in the minimum PEEQ occurs at the top of the inner rib.

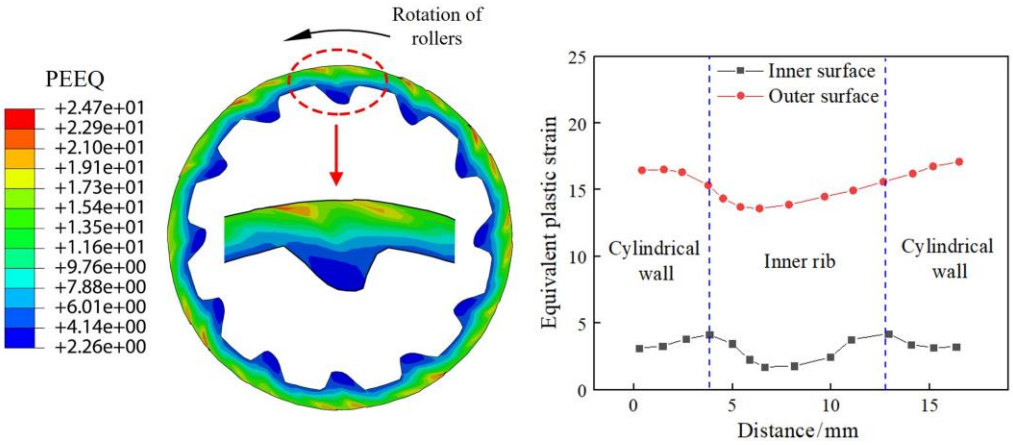

Fig. 20. PEEQ distribution at a cross-section of the spun workpiece under T=573K, f=0.4mm/r and Ψ_t=60%.

Fig. 21 shows the plastic strain distribution along three directions, where two representative elements on the middle layer of the cylindrical wall and that of the inner rib were selected. It is observed that the plastic strain begins to increase only when the rollers reach the element along with the axial movement. Moreover, a large radial compressive strain and a small tangential tensile strain can be found at the cylindrical wall (Fig. 21(a)), while a large tangential compressive strain and a small radial tensile strain exhibit at the inner ribs (Fig. 21(b)). Therefore, the radial deformation at the cylindrical wall and the tangential deformation at the inner rib are dominant for the formation of inner ribs. Additionally, a large axial tensile strain both exists at the cylindrical wall and the inner rib, which leads to not only the thinning of wall-thickness but also a low height of inner rib. Therefore, the axial deformation of material during the HBFF process of Mg alloy thin-walled CPLIRs is unfavorable for the formation of the inner rib.

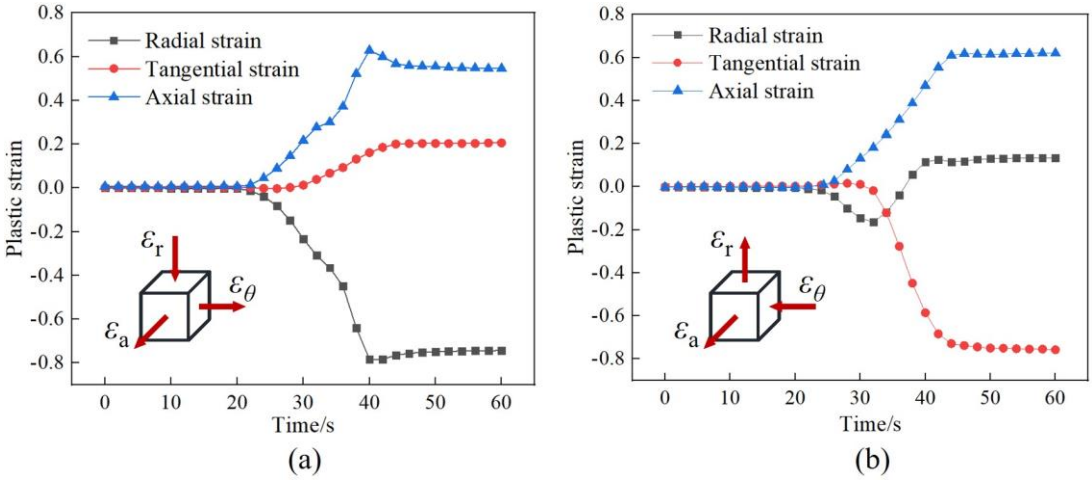

Fig. 21. Plastic strain distribution along three directions at (a) the cylindrical wall and (b) the inner rib under T=573K, f=0.4mm/r and Ψ_t=60%. (ε_a, ε_r and ε_θ denote the axial strain, radial strain and tangential strain, respectively)

3.2. Material flow of spun workpiece

It is worth noting that not only the axial and radial flow of material but also the tangential flow exists during the flow forming of thin-walled CPLIRs (Fig. 22), which plays a critical role in the filling of the rib groove. Based on the analysis above, the material suffers from axial tensile deformation at both of the cylindrical wall and the inner rib, i.e., the axial flow of material is consistent. However, there are obvious differences between the radial and the tangential deformation, and thus the radial and tangential flow of spun workpiece during HBFF is mainly discussed. Since the rollers contact the blank in the form of a counterclockwise rotation during the simulation, where the tangential component of the applied load follows the same direction and the radial component points towards the circle center (Xia et al., 2014), and the material fills the rib groove and exhibits the flow trend of counterclockwise, as shown in Fig. 23. It also can be found that the material flow at the outer layer of the blank is remarkable, while the radial and tangential flow of material gradually slows down along the wall-thickness direction due to the decrease of absolute stress values from outer surface to inner surface (Fig. 19).

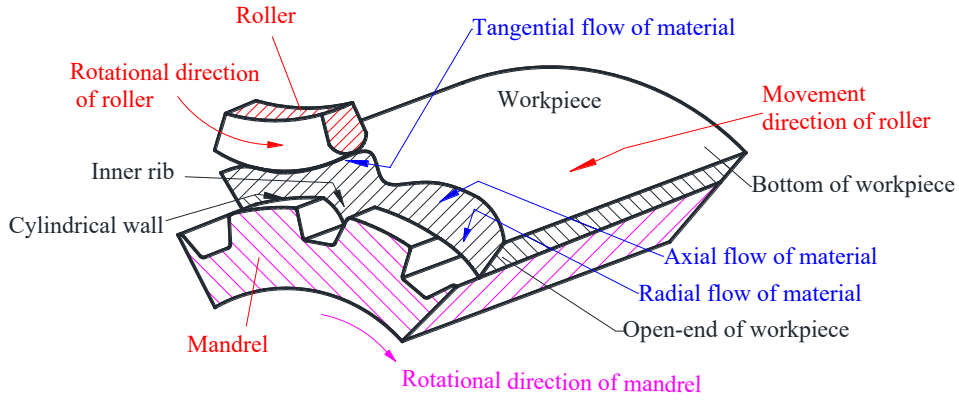

Fig. 22. Schematic illustration of material flow during flow forming of thin-walled CPLIRs.

During the HBFF of ZK61 alloy thin-walled CPLIRs, the radial compression deformation exhibits at the cylindrical wall (Fig. 21(a)), where the radial flow of material is restricted by the inner surface of the mandrel and the tangential flow can be thus greatly enhanced. As shown in Fig. 23, when the deformed material of the cylindrical wall flows into the rib area from the inflow side, the first split-flow occurs at region A, i.e., the outer layer material at the cylindrical wall flows mainly along tangential direction while the inner layer material flows into the rib groove

along tangential and radial directions. Moreover, the outer layer material at the outflow side keeps flowing forward along a tangential direction, and the second split-flow occurs at region B, i.e., one part of material at the area of the inner layer of the inner rib flows into the cylindrical wall along a tangential direction while another part flows back to the rib groove along radial as well as tangential directions. Therefore, the material flow state at the area of the outer layer of the inner rib is similar to that of the cylindrical wall. It should be noted that the tangential flow at the area of the inner layer of the inner rib is restricted by the surrounding material, while the inner surface of inner rib is a free surface, and thus the radial flow occurs easily, which plays a major role in the formation of the inner rib.

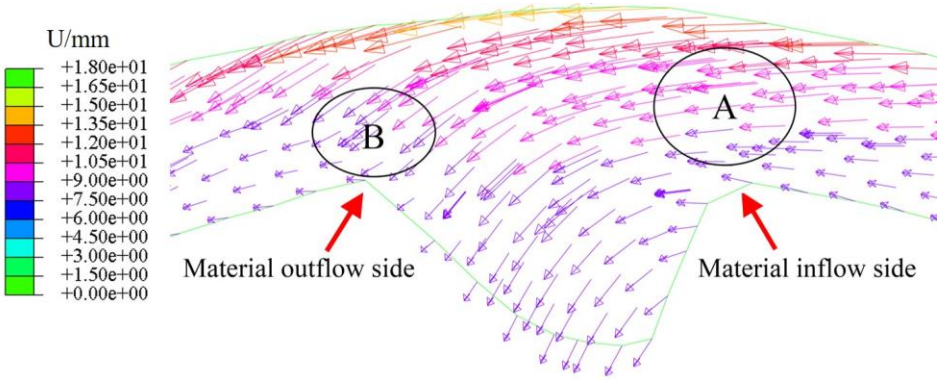

Fig. 23. Material flow state in the cross-section when T=573K, f=0.4mm/r and Ψ_t=60% (U denotes the total material displacement).

3.3. Distribution of power dissipation efficiency of spun workpiece

3.3.1. Influence of forming temperature

Fig. 24 shows the distribution of power dissipation efficiency η under different forming temperature T when ψ_t=50% and f=0.4mm/r. It can be seen that the η of each position of spun workpiece changes greatly with increasing T, which indicates that the formability of spun workpiece has high temperature sensitivity (Zhou et al., 2020). Moreover, the η value is low under T=523K due to the insufficient DRX, which increases obviously and reaches the value of about 35% under T=573K. This is because the small DRX degree can be resulted from the low T, while most of the matrix structure can be replaced by DRX grains and thus the sufficient DRX is able to be realized under T=573K. However, lots of grain boundaries were consumed and the DRX grains grow rapidly as T increases to 623K, making the DRX process slow down and the η value decreases rapidly due to the lack of nucleation sites.

Meanwhile, the twins continue to segment and refine DRX grains as T further increases to 673K, which provides nucleation sites and promotes the DRX (Long et al., 2021), and thus the η value increases again. Although η value of spun workpiece at T=573K is slightly smaller than that at T=673K under which the DRX degree is higher, the significant grain growth caused by a much higher T should be avoided during hot deformation (Srinivasan et al., 2008). Therefore, T=573K is more suitable for obtaining the good formability during HBFF of ZK61 alloy thin-walled CPLIRs.

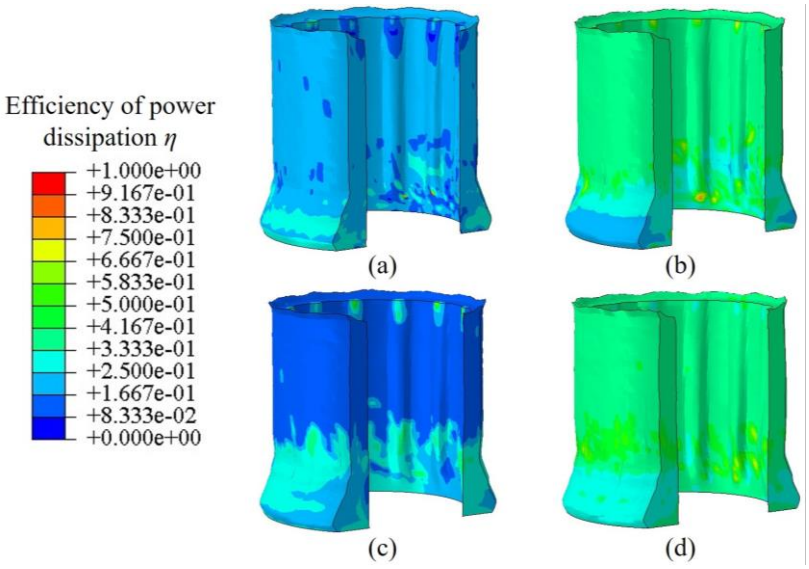

Fig. 24. Distribution of power dissipation efficiency under different temperatures when ψ_t=50% and f=0.4mm/r: (a) 523K (b) 573K (c) 623K (d) 673K.

3.3.2 Influence of roller feed rate

Fig. 25 shows the distribution of power dissipation efficiency η under different roller feed rate f when T=573K and ψ_t=50%. It can be seen that the η value of spun workpiece tends to increase with increasing f, but the local increase makes the distribution of η during the HBFF process of ZK61 alloy thin-walled CPLIRs become more uneven. This is because the material deformation in unit time increases as f increases, i.e., the strain rate of the deformed material increases which enhances the accumulation rate of the distortion energy (Xiao et al., 2018), and thus the DRX process can be facilitated and the η increases in local areas. However, the increase of strain rate will provide little time for DRX grain growth, resulting in insufficient DRX and uneven distribution of microstructure. Moreover, the small DRX grains could be formed at some local areas with high η value, where the plastic deformation is locally concentrated and the instability such as flow

localization occurs easily (Li et al., 2014). Therefore, the high f is not suitable for improving the formability of spun workpiece and the appropriate parameter can be determined as 0.4mm/r.

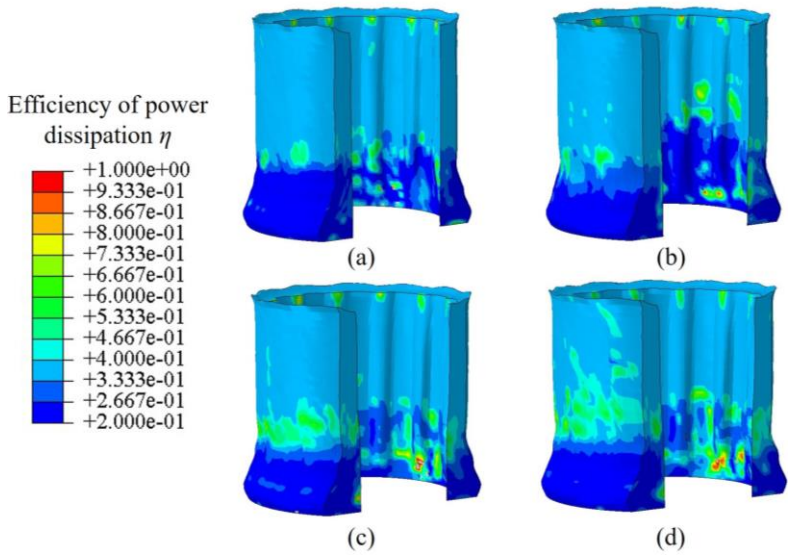

Fig. 25. Distribution of power dissipation efficiency under different f when T=573K and ψ_t=50%: (a) 0.4mm/r (b) 0.6mm/r (c) 0.8mm/r (d) 1.0mm/r.

3.3.3 Influence of thinning ratio

Fig. 26 shows the distribution of power dissipation efficiency η under different thinning ratio of wall-thickness ψ_t when f=0.4mm/r and T=573K. It can be seen that the η value of spun workpiece under all given deformation conditions is relatively high and exhibit the similar distribution at the deformed zone, and thus their formability is basically the same with the increase of ψ_t. This indicates that the complete DRX can be realized and the spun workpiece has good formability when $\psi_t \geq 50\%$ during HBFF (Zeng et al., 2019). In fact, the η value is prone to increase slightly as ψ_t increases. It is because DRX only occurs when the necessary critical strain is reached, and the thinning ratio is closely related to strain amount, i.e., the deformation degree increases significantly with increasing the ψ_t, which provides more storage energy for the dislocation movement and occurrence of DRX. Namely, the larger the thinning ratio, the more sufficient the DRX, the DRX degree tends to be higher. Moreover, the increase of thinning ratio can significantly facilitate the material flow and filling of the rib groove, leading to a higher inner rib height (Zeng et al., 2020c). Therefore, good formability of spun workpiece can be obtained under the large ψ_t ($\geqslant$50%) during the HBFF of ZK61 alloy thin-walled CPLIRs.

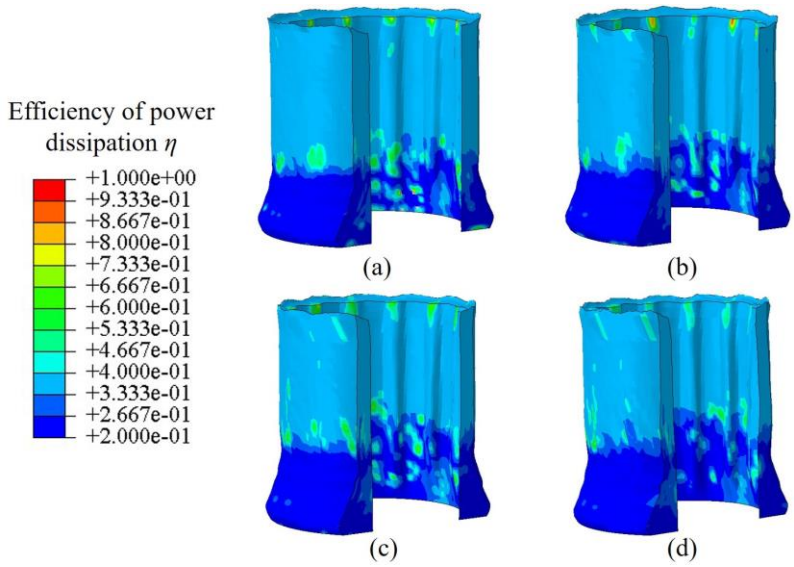

Fig. 26. Distribution of power dissipation efficiency under different ψ_t when T=573K and f=0.4mm/r: (a) 50% (b) 55% (c) 60% (d) 65%

3.4 Experimental verification

Based on the constructed 3D HPMs as well as the experimental and simulation results, the HBFF process of ZK61 alloy thin-walled CPLIRs can be optimized, and the optimal process parameter was selected as 573K, 0.4mm/r and 65%. Fig. 27 presents the formed ZK61 alloy thin-walled CPLIRs with qualified forming quality, and Fig. 28 shows variations of the evaluation indexes along the axial direction of the spun workpiece measured with the method given in Section 2.5. It can be seen that the μ decreases slightly and the λ tends to increase from the bottom end to the opening end, while the γ has no obvious change and is basically within 0.2%. This is because the material flow at the opening end has little restriction during the HBFF, and thus the axial flow occurs easily and less radial flow exists, which is responsible for the small μ and high λ near the opening end. However, the axial flow of the material at the deformation zone can be hindered by the material accumulated at the deformed zone, and thus the radial flow of the material increases gradually, which leads to the large μ and low λ near the bottom end.

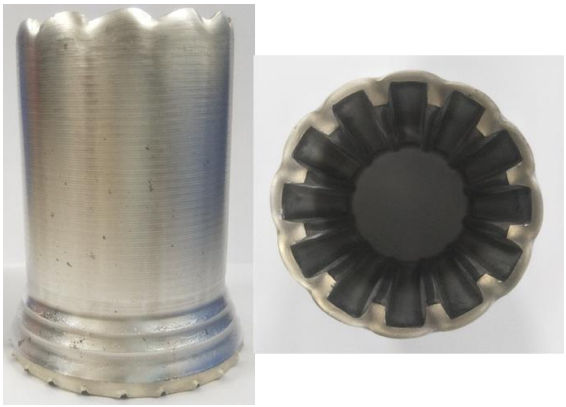

Fig. 27. ZK61 alloy thin-walled CPLIRs manufactured under T=573K, f=0.4mm/r, ψ_t=65%.

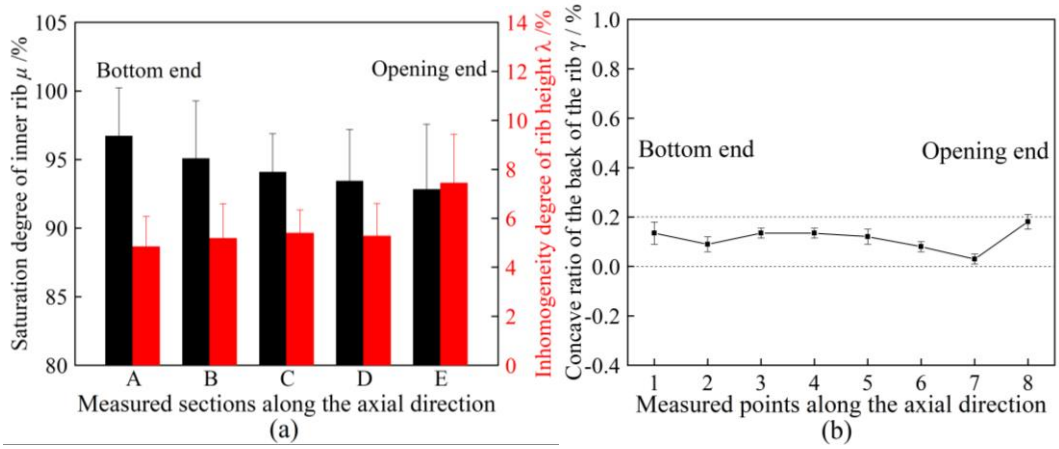

Fig. 28. Forming quality of the spun workpiece under the optimized process parameters
(a) saturation degree of inner rib μ and inhomogeneity degree of rib height λ
(b) concave ratio of the back of the rib γ.

Furthermore, the microstructure of spun workpiece was observed. Fig. 29 shows that the samples at the cylindrical wall and the inner rib were both cut for the metallographic test using an optical microscope (OM, Leica DMI5000M), the sample preparation method for OM is consistent with that of Yuan et al. (2020), i.e., the OM specimens were mechanically ground, polished and then chemically etched by a solution (1.5g picric acid, 6ml acetic acid, 10ml distilled water, 25ml ethanol) for 10s. As shown in Fig. 30, sufficient DRX occurs and a similar distribution of microstructure can be observed at both of the cylindrical wall and the inner rib, where the DRX degree is high and relatively uniform and small DRX grains were obtained. This also indicates that the high η value is beneficial for the DRX. The average DRX grain sizes of the cylindrical wall and the inner ribs assessed by the linear intercept method are 2.08μm and 2.27μm, respectively. The DRX grain size of the cylindrical wall is slightly smaller than that of the inner rib. It is because the deformation degree of the cylindrical wall is larger than that of the inner rib as analyzed in Section 4.1, and thus the grain refinement caused by DRX at the

cylindrical wall is more obvious. These further verified the simulated results.

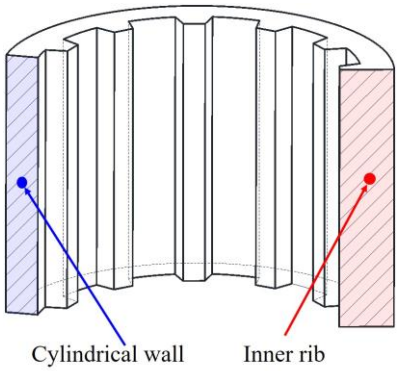

Fig. 29. Sampling for microstructural observations.

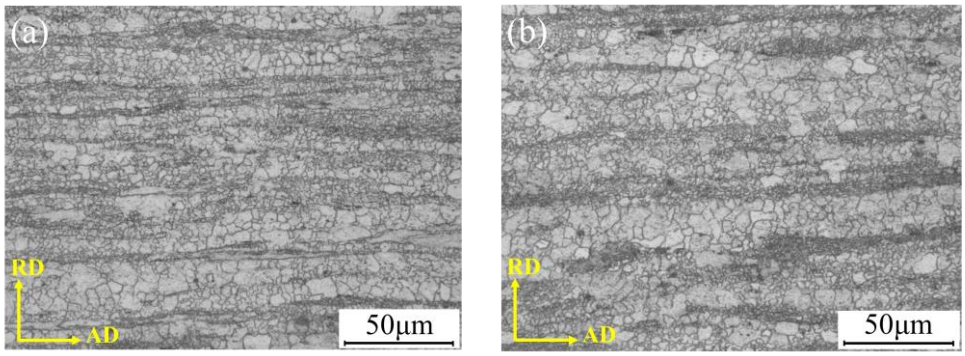

Fig. 30. Optical micrograph of spun workpiece: (a) the cylindrical wall and (b) the inner rib.

4. Conclusions

The deformation mechanism of Mg alloy cylindrical parts with longitudinal inner ribs (CPLIRs) during the hot backward flow forming (HBFF) was investigated by using the process experiment and 3D finite element (FE) simulation integrated with 3D hot processing maps (HPMs). The main conclusions were obtained as follows:

1) Considering the similar states of stress and strain, the isothermal uniaxial compression (IUC) test can be used as the physical simulation test of the HBFF of thin-walled CPLIRs, and the relationships between the large true strains and stresses of ZK61 alloy during the HBFF can be obtained by the IUC test.
2) The 3D HPMs of the ZK61 alloy at different strains were constructed on the basis of the Murty criterion, the high efficiency of power dissipation ($\eta \geq 35\%$) mainly occurs within 573 ~ 673K, 0.001-0.01s^{-1}, where the fully recrystallized microstructure can be observed. The instability region increases with increasing strain, which was related to the flow localization within 523 ~ 543K, 0.3-1s^{-1}.
3) The states of three-directional compressive stress, the tangential tensile strain at

cylindrical wall and tangential compressive strain at inner ribs are beneficial for the filling of the rib groove. The material flow at the outer layer of the inner rib is similar to that of the cylindrical wall, where the tangential flow is dominant. The large tangential flow of the inner layer material at the cylindrical wall and the radial flow of that at the inner rib play an important role in the formation of the inner rib.

4) The concavity of the outer wall at the back of the rib, the uneven distribution of the rib height along longitudinal and circumferential directions are typical defects during the HBFF of ZK61 alloy thin-walled CPLIRs. The proposed indexes including the saturation degree of the inner rib μ, the inhomogeneity degree of the rib height λ and the concave ratio of the back of the rib γ can be used to evaluate the forming quality of thin-walled CPLIRs.
5) Based on the 3D FE simulation integrated with 3D HPMs, the power dissipation efficiency of ZK61 alloy thin-walled CPLIRs during HBFF can be analyzed, which changes significantly with increasing T, the spun workpiece exhibits good formability at a small f and large ψ_t. The appropriate processing window can be determined at T=573K, f=0.4mm/r and $\psi_t \geq 50\%$, under which the spun workpiece with qualified forming quality as well as relatively uniform and fine recrystallized microstructure can be obtained.

Acknowledgments

This research is financially supported by the National Natural Science Foundation of China (No. 51775194). One of the authors, Jinchuan Long, also would like to acknowledge financial support from the China Scholarship Council (No. 201906150052) which enabled him to conduct the research at the University of Strathclyde, UK.

References

Du, Z., Jiang, S., Zhang, K., 2015. The hot deformation behavior and processing map of Ti-47.5Al-Cr-V alloy, Mater. Des. 86, 464–476.

Huang, C., Hung, J.C., Hung, C., Lin, C., 2011. Finite element analysis on neck-spinning process of tube at elevated temperature, Int. J. Adv. Manuf. Technol.

56, 1039-1048.

Jiang, S., Zheng, Y., Ren, Z., Li, C., 2009. Multi-pass spinning of thin-walled tubular part with longitudinal inner ribs. Trans. Nonferrous Met. Soc. China 19, 215-221.

Jin, Z., Li, N., Yan, K., Chen, J., Wei, D., Cui, Z., 2018. Controlling Flow Instability in Straight Spur Gear Forging Using Numerical Simulation and Response Surface Method, Acta Metall. Sin. (Engl. Lett.) 31, 82-96.

Li, J., Liu, J., Cui, Z., 2014. Characterization of hot deformation behavior of extruded ZK60 magnesium alloy using 3D processing maps. Mater. Design. 56, 889-897.

Liu, B., Zhang, Z., Jin, L., Gao, J., Dong, J., 2016. Forgeability, microstructure and mechanical properties of a free-forged Mg-8Gd-3Y-0.4 Zr alloy, Mater. Sci. Eng. A 650, 233-239.

Liu, J., Cui, Z., Li, C., 2008. Analysis of metal workability by integration of FEM and 3-D processing maps, J. Mater. Process. Technol. 205, 497-505.

Liu, J., Li, J., Cui, Z., Ou, H., Ruan, L., 2013. Material driven workability simulation by FEM including 3D processing maps for magnesium alloy, Trans. Nonferrous Met. Soc. China 23, 3011-3019.

Liu, Y., Hu, R., Li, J., Kou, H., Li, H., Chang, H., Fu, H., 2009. Characterization of hot deformation behavior of Haynes230 by using processing maps, J. Mater. Process. Technol. 209, 4020-4026.

Long, J., Xia, Q., Xiao, G., Qin, Y., Yuan, S., 2021. Flow characterization of magnesium alloy ZK61 during hot deformation with improved constitutive equations and using activation energy maps, Int. J. Mech. Sci. 191, 106069.

Ma, F., Yang, H., Zhan, M., 2010. Plastic deformation behaviors and their application in power spinning process of conical parts with transverse inner rib, J. Mater. Process. Technol. 210, 180-189.

Malik, A., Wang, Y., Cheng, H., Nazeer, F., Ahmed, B., Khan, M., Wang, M., 2020. Constitutive analysis, twinning, recrystallization, and crack in fine-grained ZK61 Mg alloy during high strain rate compression over a wide range of temperatures. Mater. Sci. Eng. A 771, 138649.

Mohamed, M., Foster, A., Lin, J., Balint, D., Dean, T., 2012. Investigation of deformation and failure features of AA6082: experimentation and modelling, Int. J.

Mach. Tools Manuf. 53, 27-38.

Murty, S., Rao, B., 1998a. Instability map for hot working of 6061 Al-10 vol%. Al_2O_3 metal matrix composite, J. Phys. D: Appl Phys. 31, 3306-3311.

Murty, S., Rao, B., 1998b. On the development of instability criteria during hot working with reference to IN 718, Mater. Sci. Eng. A 254, 76-82.

Quan, G., Ku, T., Song, W., Kang, B., 2011. The workability evaluation of wrought AZ80 magnesium alloy in hot compression, Mater. Design. 32, 2462-2468.

Ramezani, M., Neitzert, T., Pasang, T., Sellès, M., 2014. Characterization of friction behaviour of AZ80 and ZE10 magnesium alloys under lubricated contact condition by strip draw and bend test, Int. J. Mach. Tools Manuf. 85, 70-78.

Shalbafi, M., Roumina, R., Mahmudi, R., 2017. Hot deformation of the extruded Mg–10Li–1Zn alloy: Constitutive analysis and processing maps. J. Alloy. Compd. 696, 1269-1277.

Shang, X., Zhou, J., Wang, X., Lou, Y., 2015. Optimizing and identifying the process parameters of AZ31 magnesium alloy in hot compression on the base of processing maps, J. Alloy. Compd. 629, 155-161.

Slooff, F., Dzwonczyk, J., Zhou, J., Duszczyk, J., Katgerman, L., 2010. Hot workability analysis of extruded AZ magnesium alloys with processing maps, Mater. Sci. Eng. A 527, 735-744.

Srinivasan, N., Prasad, Y., Rao, P., 2008. Hot deformation behaviour of Mg–3Al alloy-a study using processing map, Mater. Sci. Eng. A 476, 146-156.

Tang, X., Shi, S., Fu, M., 2020. Interactive effect of grain size and crystal structure on deformation behavior in progressive micro-scaled deformation of metallic materials, Int. J. Mach. Tool Manufact. 148, 103473.

Wang, L., Fang, G., Leeflang, S., Duszczyk, J., Zhou. J., 2014. Investigation into the hot workability of the as-extruded WE43 magnesium alloy using processing map, J. Mech. Behav. Biomed. Mater. 32, 270-278.

Wang, S., Hou, L., Luo, J., Zhang, J., Zhuang, L., 2015. Characterization of hot workability in AA 7050 aluminum alloy using activation energy and 3-D processing map, J. Mater. Process. Technol. 225, 110-121.

Wong, C., Dean, T., Lin, J., 2004. Incremental forming of solid cylindrical components using flow forming principles, J. Mater. Process. Technol. 153-154,

60-66

Xia, Q., Xiao, G., Long, H., Cheng, X., Sheng, X., 2014. A review of process advancement of novel metal spinning. Int. J. Mach. Tools Manuf. 85, 100-121.

Xiao, G., Zhu, N., Long, J., Xia, Q., Chen, W., 2018. Research on precise control of microstructure and mechanical properties of Ni-based superalloy cylindrical parts during hot backward flow spinning, J. Manuf. Process. 34, 140-147.

Xu, W., Zhao, X., Shan, D., Li, J.M., Deng, Q., Cui, X., Li, Z.Y., 2016. Numerical simulation and experimental study on multi-pass stagger spinning of internally toothed gear using plate blank, J. Mater. Process. Technol. 229, 450-466.

Yang, Z., Xu, W., Wu, H., Wan, X., Chen, Y., Shan, D., Guo, B., 2020. Enhancing hoop strength of titanium alloy tube by cross spinning, Int. J. Mach. Tools Manuf. 152, 103530.

Yuan, S., Xia, Q., Long, J., Xiao, G., Cheng, X., 2020. Study of the microstructures and mechanical properties of ZK61 magnesium alloy cylindrical parts with inner ribs formed by hot power spinning, Int. J. Adv. Manuf. Technol. 111, 851-860.

Zeng, J., Wang, F., Dong, S., Jin, L., Fan, Y., Dong, J., 2020a. Optimization of hot backward extrusion process parameters for flat bottom cylindrical parts of Mg-8Gd-3Y alloy based on 3D processing maps, Int. J. Adv. Manuf. Technol. 108, 2149-2164.

Zeng, J., Wei, X., Dong, S., Wang, F., Jin, L., Dong, J., 2019. 3D processing maps of cast Mg-8Gd-3Y alloy at high strain rates and their application in plane strain forging, Int. J. Adv. Manuf. Technol. 106, 133-141.

Zeng, X., Fan, X., Li, H., Li, S., 2018. Flow forming process of thin-walled tubular parts with cross inner ribs, Procedia. Manuf. 15, 1239-1246.

Zeng, X., Fan, X., Li, H., Zhan, M., Li, S., Wu, K., Ren, T., 2020b. Heterogeneous microstructure and mechanical property of thin-walled tubular part with cross inner ribs produced by flow forming, Mater. Sci. Eng. A 790, 139702.

Zeng, X., Fan, X., Li, H., Zhan, M., Zhang, H., Wu, K., Ren, T., Li, S., 2020c. Die filling mechanism in flow forming of thin-walled tubular parts with cross inner ribs, J. Manuf. Process. 58, 832-844.

Zhang, R., Yu, H., Zhao, G., 2019. Role of friction in prediction and control ellipticity of high-strength casting aluminum alloy tube during hot power backward spinning, Int. J. Adv. Manuf. Technol. 102, 2709-2720.

Zhong, T., Rao, K., Prasad, Y., Gupta, M., 2013. Processing maps, microstructure evolution and deformation mechanisms of extruded AZ31-DMD during hot uniaxial compression, Mater. Sci. Eng. A 559, 773-781.

Zhou, X., Wang, K., Lu, S., Li, X., Feng, R., Zhong, M., 2020. Flow behavior and 3D processing map for hot deformation of Ti-2.7Cu alloy. J. Mater. Res. Technol. 9, 2652-2661.